Finite volume stress analysis in multi-material linear elastic body

Ž.Tuković, A.Ivanković and A.Karač

Abstract

Correct calculation of stresses at the interface of bonded or otherwise joined materials plays a significant role in many applications. It is therefore, important that traction at the material interface is calculated as accurately as possible. This paper describes procedures that can be employed to achieve this goal by using centre-based finite volume method. Total traction at the interface is calculated by decomposing it into normal and tangential components, both being calculated at each side of the interface, and applying the continuity assumption. The way in which the traction approximation is achieved depends on calculation of tangential gradient of displacement at the interface. To this end, three different methods are proposed and validated against problems with known solutions. It was shown than all methods can be successfully used to simulate problems with multi-material domains, with the procedure based on finite area method being most accurate.

1 Introduction

In the last two decades, Finite Volume (FV) method has established itself as a noteworthy alternative to the widely used finite element (FE) method for the solution of stress analysis problems. Application of both cell-centred (collocated) and vertex-centred types of the method in the stress analysis can be found in the literature. Demirdžić and co-workers pioneered application of the collocated FV method to linear-elasticity [1–4], thermo-elastoplasticity [5], thermo-viscoelasticity [6] and incompressible elasticity [7, 8]. Applications of the collocated FV method in the field of dynamic fracture problems can be attributed to Ivanković and co-workers [9–16]. Development of aforementioned procedures for stress analysis problems also opened a possibility of using the same methodology, *i.e.* cell-centred FV method in this case, for solving coupled multiphysical problems, such as fluid-structure interaction problems [17–19]. In this way, the usage of additional softwares for data transfer between different numerical methods (and softwares), eg. FV for fluid and FE for solid domain, their maintenance, *etc.*, can be avoided, thus saving computational time and producing more efficient solvers. Most important contribution to the development and application of vertex-centred FV method is due to Cross and co-workers [20–24]. Among

other contributions one should also mention work by Wheel [28–30] who has also proposed FV formulation for stress analysis in thick and thin plates [31], and Després and co-workers, who recently introduced a new cell-centred Lagrangian scheme on unstructured mesh for hyperelasticity based on Glace scheme from compressible gas dynamics [25–27].

Nevertheless, most of the aforementioned studies consider homogeneous materials and according to authors' knowledge there is no published study which would give detailed description of the FV discretisation for deformable bodies consisting of two or more dissimilar solid materials. However, joining of dissimilar materials is frequently used in mechanical engineering. Due to the difference in the (elastic) properties of the constituent materials, their interface can be the origin of stress singularities and/or discontinuities and potential source of damage onset. Since the continuum assumption is not valid across multi-material interface, discretisation of mathematical model at the interface require special care in order to prevent occurrence of physically unrealistic stresses near the interface.

This paper describes the application of collocated FV method for discretisation of multi-material linear-elastic model with special attention paid to discretisation of traction at the interface. Numerical procedure is implemented in OpenFOAM [32].

2 Mathematical model

Isothermal multi-material linear-elastic continuum by neglecting body forces is considered whose dynamic behaviour is described by linear momentum conservation law and corresponding linear elastic constitutive relation:

$$\int_V \rho \frac{\partial^2 \mathbf{u}}{\partial t^2} \, \mathrm{d}V = \oint_S \mathbf{n} \bullet \boldsymbol{\sigma} \, \mathrm{d}S, \tag{1}$$

$$\boldsymbol{\sigma} = \mu \left[\nabla \mathbf{u} + (\nabla \mathbf{u})^{\mathrm{T}} \right] + \lambda \, \mathrm{tr} \, (\nabla \mathbf{u}) \, \mathbf{I}, \tag{2}$$

where ρ is the density of elastic material, V is the volume of the continuum, $\mathbf{n}$ is the outward pointing unit normal to the surface S of the body, $\mathbf{u}$ is the displacement vector in respect to initial configuration, $\boldsymbol{\sigma}$ is the Cauchy stress tensor and μ and λ are the Lamé's coefficients:

$$\mu = \frac{E}{2(1+\nu)} \tag{3}$$

$$\lambda = \begin{cases} \dfrac{\nu E}{1-\nu^2} & \text{, for plane stress} \\ \dfrac{\nu E}{(1-2\nu)(1+\nu)} & \text{, for plane strain and 3D} \end{cases} \tag{4}$$

with ν representing Poisson's ratio.

The traction vector $\mathbf{t} = \mathbf{n}\bullet\boldsymbol{\sigma}$ on the right-hand side of Eq. (1) can be expressed in terms of displacement vector $\mathbf{u}$ using constitutive equation (2) as follows:

$$\mathbf{t} = \mathbf{n}\bullet\boldsymbol{\sigma} = \mu\mathbf{n}\bullet\nabla\mathbf{u} + \mu\nabla\mathbf{u}\bullet\mathbf{n} + \lambda\,\mathrm{tr}\,(\nabla\mathbf{u})\,\mathbf{n}. \tag{5}$$

This expression is transformed into the form which is more suitable for discretisation using collocated finite volume method, *i.e.* the traction vector is first decomposed into normal and tangential component:

$$\mathbf{t}_n = (2\mu + \lambda)\mathbf{n}\bullet\nabla\mathbf{u}_n + \lambda\mathbf{n}\,\mathrm{tr}(\nabla_t\mathbf{u}_t), \tag{6}$$

$$\mathbf{t}_t = \mu\mathbf{n}\bullet\nabla\mathbf{u}_t + \mu\nabla_t u_n, \tag{7}$$

where $\nabla_t = (\mathbf{I} - \mathbf{nn})\bullet\nabla$ is the tangential gradient operator and subscripts n and t represent the normal and tangential components of a vector, respectively. Using Eqs. (6) and (7) the traction vector can now be expressed in terms of normal and tangential derivative of displacement field:

$$\mathbf{t} = (2\mu + \lambda)\mathbf{n}\bullet\nabla\mathbf{u} - (\mu + \lambda)\mathbf{n}\bullet\nabla\mathbf{u}_t + \mu\nabla_t u_n + \lambda\mathbf{n}\,\mathrm{tr}\,(\nabla_t\mathbf{u}_t). \tag{8}$$

Momentum equation (1) with the traction defined by Eq. (8) is mathematically equivalent to the form of the model used in [33], where

$$\mathbf{t} = (2\mu + \lambda)\mathbf{n}\bullet\nabla\mathbf{u} - (\mu + \lambda)\mathbf{n}\bullet\nabla\mathbf{u} + \mu(\nabla\mathbf{u})^{\mathrm{T}} + \lambda\mathbf{n}\,\mathrm{tr}\,(\nabla\mathbf{u}). \tag{9}$$

However, a full separation of the normal derivative of displacement enables calculation of the normal derivative directly at the control-volume faces what prevents more efficiently an occurrence of checker-board oscillation pattern in the numerical solution [34]. This is especially important in the case of multi-material elastic body since region around the interface can be strong source of disturbances causing these oscillations.

The specification of the problem is completed with the definition of the domain in space and time and the initial and boundary conditions. The initial condition consists of the specified distribution of displacement $\mathbf{u}$ and velocity $\partial\mathbf{u}/\partial t$ at time zero. The boundary conditions, either constant or time varying, can be of the following type: fixed displacement, plane of symmetry and fixed traction.

3 Numerical method

Mathematical model is discretised in space using second order accurate collocated unstructured FV method while numerical integration of the model in time is performed using first order accurate implicit method. Description of discretisation procedure is divided into two parts: discretisation of the computational domain and equation discretisation.

3.1 Discretisation of the computational domain

The discretisation of the computational domain consists of the discretisation of the time interval and the discretisation of space. The time interval is split into a finite number of time-steps Δt and the equations are solved in a time-marching manner. According to unstructured FV discretisation, computational space is divided into a finite number of convex polyhedral control volumes (CV) or cells bounded by convex polygons (faces). The cells do not overlap and fill the spatial domain completely. Figure 1 shows a simple polyhedral control volume V_P around the computational point P located in its centroid, the face f, the face area S_f, the face unit normal vector $\mathbf{n}_f$ and the centroid N of the neighbouring CV sharing the face f. The geometry of the CV is fully determined by the position of its vertices.

In this study it is assumed that an interface between different elastic materials coincides with the internal CV faces. In general, however, a CV can be bounded by a combination of ordinary internal faces (f), internal faces at the multi-material interface (i) and boundary faces (b):

$$S_P = \partial V_P = \sum_f S_f + \sum_i S_i + \sum_b S_b, \tag{10}$$

where S_P is the boundary surface of a control volume V_P.

3.2 Discretisation of the mathematical model

The second-order FV discretisation of an integral conservation equation transforms the surface integrals into sums of face integrals and approximates them and the volume integrals to the second order accuracy by using the mid-point rule. Temporal discretisation is carried out by numerical integration of governing equation in time from the old time instance t^o to the new time instance $t^n = t^o + \Delta t$ using first order accurate implicit Euler scheme [34].

The fully discretised counterpart of the momentum equation (1) for the control volume V_P reads:

$$\rho_P \frac{\mathbf{u}_P^n - 2\mathbf{u}_P^o + \mathbf{u}_P^{oo}}{(\Delta t)^2} V_P = \sum_f \mathbf{t}_f^n \, S_f + \sum_i \mathbf{t}_i^n \, S_i + \sum_b \mathbf{t}_b^n \, S_b, \tag{11}$$

where the subscript P represents the cell-centre value and subscripts f, i and b represent face-centre value for internal, interface and boundary face, respectively. The superscripts n, o and oo represent values evaluated at the new time instance t^n and two previous time instances t^o and $t^{oo} = t^o - \Delta t$, respectively. As one can see from the left hand side of Eq. (11), the cell-centre acceleration is calculated using two old-time levels of displacement, thus representing a first-order accurate approximation. Following section describes the discretisation of traction for different types of CV faces.

3.2.1 Traction at internal faces

Approximation of the traction $\mathbf{t}_f^n$ at the internal CV faces which do not coincide with the multi-material interface is obtained by discretisation of Eq. (8) as follows:

$$\begin{aligned}\mathbf{t}_f^n =&(2\mu_f + \lambda_f)\mathbf{n}_f\bullet(\nabla\mathbf{u})_f^n - (\mu_f + \lambda_f)\mathbf{n}_f\bullet(\nabla\mathbf{u}_t)_f^n \\ &+ \mu_f(\nabla_t u_n)_f^n + \lambda_f\mathbf{n}_f\,\mathrm{tr}(\nabla_t\mathbf{u}_t)_f^n.\end{aligned} \tag{12}$$

The face normal derivative of displacement $\mathbf{n}_f\bullet(\nabla\mathbf{u})_f^n$ in the first term on the right-hand side of Eq (12) is discretised as follows (see [35]):

$$\mathbf{n}_f\bullet(\nabla\mathbf{u})_f^n = \underbrace{|\boldsymbol{\Delta}_f|\,\frac{\mathbf{u}_N^n - \mathbf{u}_P^n}{|\mathbf{d}_f|}}_{\text{Orthogonal contribution}} + \underbrace{(\mathbf{n}_f - \boldsymbol{\Delta}_f)\bullet(\nabla\mathbf{u})_f^n}_{\text{Non-orthogonal correction}}, \tag{13}$$

where $\boldsymbol{\Delta}_f = \mathbf{d}_f/(\mathbf{d}_f\bullet\mathbf{n}_f)$ (see Fig. 1). The orthogonal contribution in Eq. (13) is treated implicitly, while the non-orthogonal correction is explicit[1]. Discretisation procedure defined by expression (13) is also applied to the face normal derivative of tangential displacement $\mathbf{n}_f\bullet(\nabla\mathbf{u}_t)_f$ in the second term on the right-hand side of Eq. (12).

Last two terms on the right-hand side of Eq. (12) as well as non-orthogonal corrections in the first two terms are treated as explicit after discretisation and for their calculation tangential gradient of displacement field is needed at the CV faces. The face-centre gradient of displacement is calculated by linear interpolation of the neighbouring cell-centre values,

$$(\nabla\mathbf{u})_f = f_x(\nabla\mathbf{u})_P + (1 - f_x)(\nabla\mathbf{u})_N, \tag{14}$$

where $f_x = \overline{fN}/\overline{PN}$ is the interpolation factor. The cell-centre gradient of displacement is calculated using discretised Gauss integral theorem,

$$(\nabla\mathbf{u})_P = \frac{1}{V_P}\sum_f \mathbf{n}_f\mathbf{u}_f S_f, \tag{15}$$

where $\mathbf{u}_f$ is the face-centre displacement which is calculated by linear interpolation of the neighbouring cell-centre values. Equation (15) will give a second order accurate approximation of cell-centre gradient if face-centre displacement is calculated with second order accuracy. Simple linear interpolation (see Eq.(14)) will give second order approximation of variable in face centre only if line $\overline{PN}$ intersects face f in its centroid. Otherwise linear interpolation with "skewness" correction must be applied, *i.e.*

$$\mathbf{u}_f = f_x\mathbf{u}_P + (1 - f_x)\mathbf{u}_N + \mathbf{m}_f\bullet(\nabla\mathbf{u})_f, \tag{16}$$

[1]Here, term explicit means that the expression will be evaluated using displacement field from the previous iteration and it will contribute to the right-hand side of the resultant linear algebraic equation.

where $\mathbf{m}_f$ is the skewness correction vector, which points from the intersection point between the line $\overline{PN}$ and the face f to the face centre, as shown in Fig.1.

The cell-centre displacement gradient needed for skewness and non-orthogonal correction and all other explicit terms in the discretised momentum equation are used from previous outer iteration.

3.2.2 Traction at the interface

Approximation of traction vector $\mathbf{t}_i^n$ at the internal CV faces coinciding with the multi-material interface must be derived with a special care. Since the normal derivative of displacement is discontinuous across the interface, expression (8) is valid only up to the interface. Taking that into account and using the fact that displacement and traction must be continuous across the interface, approximation of the traction will be derived in such a way to ensure physically realistic solution near the interface and reasonable convergence properties of the solution procedure.

Figure 2 shows control volumes V_P and V_{Ni} with the common face i at the interface between two different elastic materials. Different properties at the two sides of the interface are designated with the subscripts ia and ib where side ia of the interface belongs to control volume V_P. Derivation of traction approximation at the centre of the face i is carried out separately for the normal and tangential component. Normal component of the traction defined by Eq. (6) is discretised separately at the left and right side of the interface as follows:

$$(\mathbf{t}_n)_{ia} = (2\mu_{ia} + \lambda_{ia})\frac{(\mathbf{u}_n)_i - (\mathbf{u}_n)_P}{\delta_{an}} + \lambda_{ia}\mathbf{n}_i \operatorname{tr}(\nabla_t \mathbf{u}_t)_{ia}, \tag{17}$$

$$(\mathbf{t}_n)_{ib} = (2\mu_{ib} + \lambda_{ib})\frac{(\mathbf{u}_n)_{Ni} - (\mathbf{u}_n)_i}{\delta_{bn}} + \lambda_{ib}\mathbf{n}_i \operatorname{tr}(\nabla_t \mathbf{u}_t)_{ib}, \tag{18}$$

where it is assumed that mesh is orthogonal at the face i. Taking into account continuity of traction across the interface, $(\mathbf{t}_n)_{ia} = (\mathbf{t}_n)_{ib}$, one can express the normal component of displacement vector at the face i by combining Eqs. (17) and (18) as:

$$\begin{aligned}(\mathbf{u}_n)_i =& \frac{(2\mu_{ia} + \lambda_{ia})\delta_{bn}(\mathbf{u}_n)_P + (2\mu_{ib} + \lambda_{ib})\delta_{an}(\mathbf{u}_n)_{Ni}}{(2\mu_{ia} + \lambda_{ia})\delta_{bn} + (2\mu_{ib} + \lambda_{ib})\delta_{an}} \\ &+ \frac{\delta_{an}\delta_{bn}\left[\lambda_{ib}\mathbf{n}_i \operatorname{tr}(\nabla_t \mathbf{u}_t)_{ib} - \lambda_{ia}\mathbf{n}_i \operatorname{tr}(\nabla_t \mathbf{u}_t)_{ia}\right]}{(2\mu_{ia} + \lambda_{ia})\delta_{bn} + (2\mu_{ib} + \lambda_{ib})\delta_{an}}.\end{aligned} \tag{19}$$

where δ_{an} and δ_{bn} are distances between cell centres of control volumes V_P and V_{Ni} and common face, respectively, as shown in Fig.2.

This expression can be further simplified by taking into account continuity of the tangential gradient across the interface, *i.e.* $(\nabla_t \mathbf{u})_{ia} = (\nabla_t \mathbf{u})_{ib}$. However, this will not be done at this stage in order to leave a possibility to analyse different approaches for calculation of tangential gradient at the interface. Substituting

Eq. (19) into Eq. (17), a final expression for the approximation of the normal traction is obtained:

$$\begin{aligned}(\mathbf{t}_n)_i =& \overline{(2\mu+\lambda)}_i \frac{(\mathbf{u}_n)_{Ni} - (\mathbf{u}_n)_P}{\delta_{in}} \\ &+ \frac{(2\mu_{ia}+\lambda_{ia})\delta_{bn}\lambda_{ib}\mathbf{n}_i \operatorname{tr}(\nabla_t \mathbf{u}_t)_{ib} + (2\mu_{ib}+\lambda_{ib})\delta_{an}\lambda_{ia}\mathbf{n}_i \operatorname{tr}(\nabla_t \mathbf{u}_t)_{ia}}{(2\mu_{ia}+\lambda_{ia})\delta_{bn} + (2\mu_{ib}+\lambda_{ib})\delta_{an}},\end{aligned} \tag{20}$$

where $\delta_{in} = \delta_{an} + \delta_{bn}$ and $\overline{(2\mu+\lambda)}_i$ is the material property at the interface obtained by so-called harmonic interpolation:

$$\overline{(2\mu+\lambda)}_i = \frac{(2\mu_{ia}+\lambda_{ia})(2\mu_{ib}+\lambda_{ib})}{\frac{\delta_{bn}}{\delta_{in}}(2\mu_{ia}+\lambda_{ia}) + \frac{\delta_{an}}{\delta_{in}}(2\mu_{ib}+\lambda_{ib})}. \tag{21}$$

Applying the same procedure for the tangential component of traction, following expressions for the tangential displacement and traction are obtained:

$$\begin{aligned}(\mathbf{u}_t)_i =& \frac{\mu_{ia}\delta_{bn}(\mathbf{u}_t)_P + \mu_{ib}\delta_{an}(\mathbf{u}_t)_{Ni}}{\mu_{ia}\delta_{bn} + \mu_{ib}\delta_{an}} \\ &+ \frac{\delta_{an}\delta_{bn}\left[\mu_{ib}(\nabla_t u_n)_{ib} - \mu_{ia}(\nabla_t u_n)_{ia}\right]}{\mu_{ia}\delta_{bn} + \mu_{ib}\delta_{an}},\end{aligned} \tag{22}$$

$$\begin{aligned}(\mathbf{t}_t)_i =& \overline{\mu}_i \frac{(\mathbf{u}_t)_{Ni} - (\mathbf{u}_t)_P}{\delta_{in}} \\ &+ \frac{\mu_{ia}\mu_{ib}\delta_{bn}(\nabla_t u_n)_{ib} + \mu_{ib}\mu_{ia}\delta_{an}(\nabla_t u_n)_{ia}}{\mu_{ia}\delta_{bn} + \mu_{ib}\delta_{an}},\end{aligned} \tag{23}$$

where $\overline{\mu}_i$ is a Lamé's coefficient at the interface obtained by harmonic interpolation:

$$\overline{\mu}_i = \frac{\mu_{ia}\mu_{ib}}{\frac{\delta_{bn}}{\delta_{in}}\mu_{ia} + \frac{\delta_{an}}{\delta_{in}}\mu_{ib}} \tag{24}$$

By summing Eqs. (20) and (23), the final expression for the interface traction is obtained:

$$\begin{aligned}\mathbf{t}_i =& \overline{(2\mu+\lambda)}_i \frac{\mathbf{u}_{Ni} - \mathbf{u}_P}{\delta_{in}} - \left[\overline{(2\mu+\lambda)}_i - \overline{\mu}_i\right] \frac{(\mathbf{u}_t)_{Ni} - (\mathbf{u}_t)_P}{\delta_{in}} \\ &+ \frac{(2\mu_{ia}+\lambda_{ia})\delta_{bn}\lambda_{ib}\mathbf{n}_i \operatorname{tr}(\nabla_t \mathbf{u}_t)_{ib} + (2\mu_{ib}+\lambda_{ib})\delta_{an}\lambda_{ia}\mathbf{n}_i \operatorname{tr}(\nabla_t \mathbf{u}_t)_{ia}}{(2\mu_{ia}+\lambda_{ia})\delta_{bn} + (2\mu_{ib}+\lambda_{ib})\delta_{an}} \\ &+ \frac{\mu_{ia}\mu_{ib}\delta_{bn}(\nabla_t u_n)_{ib} + \mu_{ib}\mu_{ia}\delta_{an}(\nabla_t u_n)_{ia}}{\mu_{ia}\delta_{bn} + \mu_{ib}\delta_{an}},\end{aligned} \tag{25}$$

where the first term on the right-hand side is treated as implicit and remaining terms are explicit. One can note that in the case of equal materials at the two sides of the interface, Eq. (25) is reduced to Eq. (12) and Eqs. (19) and (22) are reduced to the linear interpolation formula.

3.2.3 Calculation of tangential gradient of displacement at the interface

Application of Eqs. (19), (22) and (25) require evaluation of the tangential gradient of displacement at the interface. Three different procedures are proposed. The simplest approach is based on the application of already calculated gradients in the neighbouring cell centres. In that sense, two different procedures can be used. In the first procedure, tangential gradient of displacement at the interface is extrapolated from the neighbouring cell centres, *i.e.*

$$(\nabla_t \mathbf{u})_{ia} = (\mathbf{I} - \mathbf{n}_i \mathbf{n}_i)_{\bullet} (\nabla \mathbf{u})_P, \tag{26}$$

$$(\nabla_t \mathbf{u})_{ib} = (\mathbf{I} - \mathbf{n}_i \mathbf{n}_i)_{\bullet} (\nabla \mathbf{u})_{Ni}. \tag{27}$$

and the procedure is referred to as *extrapolated* method. Using this procedure discontinuity of the tangential gradient is present across the interface but it tends to zero with the mesh refinement. In the second procedure, tangential gradient is calculated using linear interpolation of the neighbouring cell values, representing the *interpolated* method, *i.e.*

$$(\nabla_t \mathbf{u})_{ia} = (\nabla_t \mathbf{u})_{ib} = (\mathbf{I} - \mathbf{n}_i \mathbf{n}_i)_{\bullet} \left[f_x (\nabla \mathbf{u})_P + (1 - f_x)(\nabla \mathbf{u})_{Ni} \right]. \tag{28}$$

This procedure forces the continuity of the tangential gradient across the interface but the use of linear interpolation is dubious since normal derivative of tangential gradient is discontinuous across the interface.

The third approach is to calculate tangential gradient of displacement directly at the interface. Let the interface be represented by the surface mesh consisting of the arbitrary polygonal control areas (faces). In this approach, one has to calculate the face-centre tangential gradient of displacement using face-centre displacements given by Eqs. (19) and (22). For this purpose, the surface Gauss' integral theorem is used, which, for a displacement $\mathbf{u}$ defined on surface S bounded by closed line ∂S, reads as follows [36, 37]:

$$\int_S \nabla_t \mathbf{u} \, \mathrm{d}S = \int_{\partial S} \mathbf{m}\mathbf{u} \, \mathrm{d}L - \int_S \kappa \, \mathbf{n}\mathbf{u} \, \mathrm{d}S, \tag{29}$$

where $\mathbf{n}$ is the unit normal vector on the surface S, $\mathbf{m}$ is the unit bi-normal vector perpendicular to a line ∂S and tangential to surface S and κ is the mean curvature of the interface.

Approximation of the face-centre tangential gradient of displacement is obtained by discretising Eq. (29) on the control area S_i (see Fig. 3) using basic principles of the finite volume discretisation procedure. Thus, tangential gradient of displacement at the centroid of control area S_i is calculated using the following expression:

$$(\nabla_t \mathbf{u})_i = \frac{1}{S_i} \sum_e \mathbf{m}_e \mathbf{u}_e L_e - \kappa_i \mathbf{n}_i \mathbf{v}_i, \tag{30}$$

where surface integrals over the control area S_i and line integrals over the control area edge e of length L_e are approximated using the mid-point rule. Subscript

e implies the value of the variable in the middle of the edge e and summation is performed over all edges closing the face i. The mean curvature at the control-area centre is calculated as follows:

$$\kappa_i = \frac{1}{S_i} \sum_e \mathbf{m}_e L_e. \tag{31}$$

The edge-centre displacement $\mathbf{u}_e$ is calculated using the following linear interpolation formula:

$$\mathbf{u}_e = (\mathbf{T}_e)^T_{\bullet} \left[e_x \mathbf{T}_{P\bullet} \mathbf{u}_P + (1 - e_x) \mathbf{T}_{N\bullet} \mathbf{u}_N \right], \tag{32}$$

where e_x is the interpolation factor calculated as the ratio of geodetic distances $\overline{eN}$ and $\overline{PeN}$ (see Fig. 4):

$$e_x = \frac{\overline{eN}}{\overline{PN}}, \tag{33}$$

and $\mathbf{T}_P$, $\mathbf{T}_N$ and $\mathbf{T}_e$ are the tensors of transformation from the global Cartesian coordinate system to the edge-based local orthogonal coordinate system, as defined in Fig. 4.

The above described finite volume discretisation procedure intended for discretisation on curved surface mesh is refereed to as *the finite area method* (FAM). More details on this method can be found in [38, 39].

3.2.4 Traction at boundary faces

Approximation of the traction at the boundary faces depends on the specified boundary condition. For example, in case of specified displacement, traction is approximated using following expression:

$$\begin{aligned} \mathbf{t}_b^n =& (2\mu_b + \lambda_b) \frac{\mathbf{u}_b^n - \mathbf{u}_P^n}{\delta_n} - (\mu_b + \lambda_b) \frac{(\mathbf{u}_t)_b^n - (\mathbf{u}_t)_P^n}{\delta_n} \\ &+ \mu_b (\nabla_t u_n)_b^n + \lambda_b \mathbf{n}_b \operatorname{tr}(\nabla_t \mathbf{u}_t)_b^n, \end{aligned} \tag{34}$$

where subscript b represents values at the CV boundary faces and δ_n is the normal distance between neighbouring cell-centre and boundary face. Tangential gradient of displacement is extrapolated from neighbouring cell.

On the other hand, in the case of specified traction at the boundary face, Eq. (34) is used to calculate displacement $\mathbf{u}_b^n$ needed for calculation of displacement gradient.

3.2.5 Resulting linear algebraic equation

Applying described discretisation of traction for the different types of CV faces, Eq. (11) can be written in the form of linear algebraic equation which relates the value of the unknown variable at the CV centre with the values at the centres of the neighbouring CVs. Such linear algebraic equation assembled for cell P reads:

$$a_P \mathbf{u}_P^n + \sum_N a_N \mathbf{u}_N^n + \sum_{Ni} a_{Ni} \mathbf{u}_{Ni}^n = \mathbf{r}_P^n, \tag{35}$$

where one should distinguish ordinary neighbouring cells N and neighbouring cells Ni sharing faces at the multi-material interface with the considered cell P. Diagonal coefficient a_P, neighbour coefficients $a_{N(i)}$ and source term $\mathbf{r}_P$ are defined by following expressions:

$$a_P = \frac{\rho_P V_P}{(\Delta t)^2} + \sum_f (2\mu_f + \lambda_f)\frac{|\mathbf{\Delta}_f|}{|\mathbf{d}_f|}S_f + \sum_i \overline{(2\mu+\lambda)}_i \frac{1}{\delta_{in}} S_i, \tag{36}$$

$$a_N = -(2\mu_f + \lambda_f)\frac{\mathbf{\Delta}_f}{|\mathbf{d}_f|}S_f, \quad a_{Ni} = -\overline{(2\mu+\lambda)}_i \frac{1}{\delta_{in}} S_i, \tag{37}$$

$$\begin{aligned}
\mathbf{r}_P^n = {} & \rho_P V_P \left(\frac{2\mathbf{u}_P^o}{(\Delta t)^2} - \frac{\mathbf{u}_P^{oo}}{(\Delta t)^2} \right) + \sum_f (2\mu_f + \lambda_f)(\mathbf{n}_f - \mathbf{\Delta}_f)\bullet(\nabla \mathbf{u})_f^n S_f \\
& - \sum_f (\mu_f + \lambda_f) \left[|\mathbf{\Delta}_f| \frac{(\mathbf{u}_t)_N^n - (\mathbf{u}_t)_P^n}{|\mathbf{d}_f|} + (\mathbf{n}_f - \mathbf{\Delta}_f)\bullet(\nabla \mathbf{u}_t)_f^n \right] S_f \\
& + \sum_f \mu_f \mathbf{n}_f \bullet (\nabla_t u_n)_f \, S_f + \sum_f \lambda_f \mathbf{n}_f \, \mathrm{tr}\left[(\nabla_t \mathbf{u}_t)_f\right] S_f \\
& - \sum_i \left[\overline{(2\mu+\lambda)}_i - \overline{\mu}_i \right] \frac{(\mathbf{u}_t)_{Ni} - (\mathbf{u}_t)_P}{\delta_{in}} \\
& + \sum_i \frac{(2\mu_{ia} + \lambda_{ia})\delta_{bn}\lambda_{ib}\mathbf{n}_i \, \mathrm{tr}(\nabla_t \mathbf{u}_t)_{ib} + (2\mu_{ib} + \lambda_{ib})\delta_{an}\lambda_{ia}\mathbf{n}_i \, \mathrm{tr}(\nabla_t \mathbf{u}_t)_{ia}}{(2\mu_{ia} + \lambda_{ia})\delta_{bn} + (2\mu_{ib} + \lambda_{ib})\delta_{an}} \\
& + \sum_i \frac{\mu_{ia}\mu_{ib}\delta_{bn}(\nabla_t u_n)_{ib} + \mu_{ib}\mu_{ia}\delta_{an}(\nabla_t u_n)_{ia}}{\mu_{ia}\delta_{bn} + \mu_{ib}\delta_{an}},
\end{aligned} \tag{38}$$

where the contribution from the boundary faces, depending on the specified boundary conditions, is omitted.

3.3 Solution procedure

Equation (35) is assembled for each CV in the mesh resulting in the system of algebraic equations:

$$[A][\mathbf{u}] = [\mathbf{r}], \tag{39}$$

where $[A]$ is the sparse square matrix with coefficients a_P on the diagonal and $a_{N(i)}$ off the diagonal, $[\mathbf{u}]$ is the displacement vector consisting of displacements for all computational points, and $[\mathbf{r}]$ is the right-hand side vector consisting of $\mathbf{r}_P^n$ terms for all CVs. The above system is solved for the three components of $\mathbf{u}$ in a segregated manner.

Solution procedure consists of following steps:

1. Switch to the new time step and initialize the value of dependent variable with the value from the previous time step;

2. Calculate face-centre displacement for the internal faces using linear interpolation formula (16) and for the faces at the multi-material interface using Eqs. (19) and (22);

3. Calculate cell-centre gradient using Eq. (15) with face-centre displacement obtained in the previous step;

4. Calculate face-centre gradient using linear interpolation (or using special procedure for the faces at the interface)

5. Assemble and solve Eq. (39) for displacement $\mathbf{u}$;

6. Return to step 1 if converged solution is reached, otherwise return to step 2.

The matrix $[A]$ from Eq. (39) is symmetric and diagonally dominant even in the absence of the transient term, which is important for steady-state calculations. In this work, the system of equations is solved using the incomplete Cholesky conjugate gradient solver (ICCG) [40].

It has to be mentioned that the discretised system described above includes some explicit terms, depending on the displacement from the previous iteration. Therefore, it would be unnecessary to converge the solution of Eq. (39) to a very tight tolerance, as the new solution will only be used to update the explicit terms. Only when the solution changes less than some predefined tolerance the system is considered to be solved. In transient calculations, this is done for every time-step, using the previously available solution as the initial guess.

4 Validation examples

In order to validate implemented procedures, three different test cases with known solutions are considered. Namely, a thick-walled bi-material cylinder subjected to both internal pressure and tangential loading, and multi-material plate loaded in tension are simulated and results compared to those available in literature.

4.1 A bi-material thick-walled cylinder - internally pressurised

Figure 5a shows a bi-material thick-walled cylinder with associated dimensions and boundary conditions (similar problem was analysed in [41]). The problem is considered as plane stress, with a quarter of domain modelled due to symmetry for the sake of generality (the case can also be considered as axi-symmetric, ie. one-dimensional.). Number of cells is set to 120 circumferentially and 50 radially. The case is simulated as steady-state, with constant pressure, p_i, applied to inner bore surface. Outside surface is modelled as stress-free, and left and bottom boundaries as symmetry planes. Material properties are associated with

two distinguished areas given in the figure, with constant Poisson's ratios of $\nu_1 = 0.35$ and $\nu_2 = 0.3$ for all simulations, and E_2/E_1 varying from 0.2 to 10.

Comparison between numerical and analytical solutions is performed in terms of circumferential and radial stresses in radial direction through cylinder, for which analytical solutions are as follows:

$$\sigma_r(r) = \begin{cases} \dfrac{r_1^2 p_i - r_2^2 p_{12} + (p_{12} - p_i)\left(\dfrac{r_1 r_2}{r}\right)^2}{r_2^2 - r_1^2} & , r_1 \leq r < r_2 \\ \dfrac{r_2^2 p_{12} - p_{12}\left(\dfrac{r_2 r_3}{r}\right)^2}{r_3^2 - r_2^2} & , r_2 < r \leq r_3 \end{cases} \tag{40}$$

$$\sigma_\theta(r) = \begin{cases} \dfrac{r_1^2 p_i - r_2^2 p_{12} - (p_{12} - p_i)\left(\dfrac{r_1 r_2}{r}\right)^2}{r_2^2 - r_1^2} & , r_1 \leq r < r_2 \\ \dfrac{r_2^2 p_{12} + p_{12}\left(\dfrac{r_2 r_3}{r}\right)^2}{r_3^2 - r_2^2} & , r_2 < r \leq r_3 \end{cases} \tag{41}$$

where pressure at the interface, p_{12} is given as:

$$p_{12} = \frac{\dfrac{2 r_1^2 p_i}{E_1(r_2^2 - r_1^2)}}{\dfrac{1}{E_2}\left(\dfrac{r_3^2 + r_2^2}{r_3^2 - r_2^2} + \nu_2\right) + \dfrac{1}{E_1}\left(\dfrac{r_2^2 + r_1^2}{r_2^2 - r_1^2} - \nu_1\right)} \tag{42}$$

Figure 6 shows comparison between analytical and numerical solution at the interface for $E_2/E_1 = 10$, when no special treatment in traction calculation at the interface is carried out. It can be seen that results agree well overall, but stress peaks are present at and near interface (in cells next to the interface). This is a big drawback for the problems where stresses at the interface are important, such as interfacial crack propagation. Stress peak magnitude could be reduced using finer mesh next to the interface, but success is not guaranteed, especially for complex interface shapes where necessary mesh refinement cannot be easily achieved.

On the other hand, Fig.7 shows comparison between numerically calculated stresses and analytical solutions using developed procedures. Only results using extrapolated method are shown, but interpolated and FAM methods produce almost identical results for this particular problem and relatively coarse mesh. It can be seen that the agreement with analytical solution is excellent for all E_2/E_1 ratios, with overall error being less than 1% for the mesh used and adopted accuracy when solving resulting set of equations (set to 10^{-9}).

4.2 A bi-material thick-walled cylinder - tangential traction applied

Next example has identical geometry to the previous one, except tangential load is applied along external surface, whereas the inner bore surface is fixed, as

shown in Fig.5b. Since axi-symmetry is not complied in terms of loading, the whole geometry is modelled, with 480 cells circumferentially, and 50 in radial direction. Analytical solution for this problem is based on work by Nie and Batra [42], where they treated plane strain deformation of hollow nonhomogeneous cylinders subjected to various boundary conditions. They showed that radial and circumferential stresses are equal zero for any material distribution, whereas shear stress distribution is given as

$$\sigma_{r\theta}(r) = \tau \frac{r_3^2}{r^2} \tag{43}$$

and does not depend on shear modulus. Applying their procedure to a bi-meterial compound cylinder, one can obtain radial displacements to be zero, and the expression for circumferential displacement in radial direction as follows (see Appendix A for more details):

$$u_\theta(r) = \begin{cases} \dfrac{\tau r_3^2}{2\mu_1}\left(\dfrac{r}{r_1^2} - \dfrac{1}{r}\right) & , r_1 \leq r < r_2 \\ \dfrac{\tau r_3^2}{2}\left[\left(\dfrac{1}{\mu_1 r_1^2} - \dfrac{1}{\mu_1 r_2^2} + \dfrac{1}{\mu_2 r_2^2}\right) r - \dfrac{1}{\mu_2}\dfrac{1}{r}\right] & , r_2 \leq r \leq r_3 \end{cases} \tag{44}$$

Figure 8 shows comparison between numerical predictions (only extrapolated method) and aforementioned analytical solutions. Again, an excellent agreement is achieved for all E_2/E_1 ratios using all procedures for traction calculation at the interface.

4.3 A multi-material plate

The third test case considers a problem of free-edge stress singularity near the interaction of the free surface and the interface of bonded materials. The case geometry is shown in Fig.9a with associated mesh in Fig.9b. The only variable geometry parameter is the mid-layer thickness, h, being 0, $0.002W$, $0.005W$ and $0.01W$, where $2W$ is the specimen width. Number of cells in y direction is 240 for all cases and material domains, with 120 cells in x direction for material domains 1 and 2. Number of cells in x direction of the mid-layer depends on thickness and is equal to 0 for $h = 0$, 250 for $h = 0.002W$ and $h = 0.005W$, and 500 for $h = 0.01W$. The reason for such a high number of cells was to have the cell aspect ratio near the edge and the interface closer to 1. Apart from the mid-layer, where uniform mesh distribution is used, the specimen is meshed using so-called geometrical distribution with aspect ratio between the last and first cell size in each direction equal to 10000, to ensure very fine mesh near the interface and free edge (order of μm), as indicated in Fig.9b, providing more computational points/cells in log-log plot as discussed below.

This problem is analysed in details in [43] using two sets of material properties. Here, however, only the first set is analysed with properties given in Table 1. In short, a two-dimensional plate is subjected to tensile stress σ_0 at the left boundary, whereas the right boundary is modelled as symmetry plane. Due to

symmetry, the upper boundary is also modelled as symmetry plane, whereas other boundaries are stress free. Following the analysis by Ioka et al. [43] normal stresses, σ_{xx}, along interfaces between materials 1 and 3 (interface 13), and 2 and 3 (interface 23), are monitored, for four different mid-layer thicknesses.

Figure 10 shows comparison between calculated stress distributions using extrapolated method with results from [43], where boundary element method (BEM) was used. As can be seen, the differences between methods are negligible. Simulations produce a r^{-p}-type singularity in the vicinity of the interaction of free surface and interface, typical for this kind of problem. Here, p stands for the exponent of free-edge stress singularity and can be obtained analytically by solving following characteristic equation (eg. [44]):

$$\begin{aligned}\lambda^2(\lambda^2-1)\alpha^2+2\lambda^2[\sin^2(\pi\lambda/2)-\lambda^2]\alpha\beta \\ +[\sin^2(\pi\lambda/2)-\lambda^2]\beta^2+\sin^2(\pi\lambda/2)\cos^2(\pi\lambda/2)=0\end{aligned} \tag{45}$$

where

$$Re(\lambda)=1-\omega \tag{46}$$

and

$$\begin{aligned}\alpha&=\frac{m_2-km_1}{m_2+km_1}\\ \beta&=\frac{(m_2-2)-k(m_1-2)}{m_2+km_1}\end{aligned} \tag{47}$$

are Dundurs' parameters, with $k=\mu_2/\mu_1$ and $m_i=4(1-\nu_i)$ for plane strain. For example, in the absence of the mid-layer, using Eq. (45) one can obtain $p_{12}=0.09336$ whereas finite-volume method predicts the value of $p_{12}=0.09347$ via nonlinear regression of calculated stress profile along the interface. Similarly to previous two examples, there is no much difference between three proposed methods for calculating tangential gradients in terms of stress profiles along the interfaces for chosen mesh densities, as shown in Fig.11 for the case with $h=0.01W$. However, as noted earlier, the mesh in the mid-layer is very fine, thus increasing the accuracy of gradient calculations in the interfaces' regions, and potentially reducing the differences between methods.

Let us now examine the same case with a coarser mesh, with the number of cells in domains 1 and 2 as earlier, except a uniform meshing strategy is employed, *i.e.* cells have the same aspect ratio throughout these domains. On the other hand, the number of cells in mid-layer in x direction is decreased from 500 to 10. Figure 12 shows stress distribution along interfaces 13 and 23 for three different methods with results from previous simulations using finer mesh. As can be seen, there is no much difference between methods, except in the region for $r/W<0.1$. For smaller values of r/W, the interpolated method deviate from finer-mesh results both in value and trend, whereas the extrapolated and FAM methods have similar results and follow nicely finer-mesh results up to the last cell. This is, however, expected since the size of the cell in y direction was similar to the thickness of mid-layer, so free-edge singularity

could not be picked-up. If the stress distribution along horizontal line in the region where all three methods do not differ much, *e.g.* 15 mm from the free edge (and upper symmetry plane) is plotted, as in Fig.13a, there is no obvious difference between methods. However, when the region around mid-layer is magnified, as given in Fig.13b, one can notice deviations from stress continuity for extrapolated and interpolated methods in the cells next to the interfaces, whereas the FAM method follows physically realistic, continuous trend.

According to presented results, it appears that three methods differ in accuracy, what is to be investigated next. To this end, simpler bi-material plate cases ($h = 0$), to avoid interface interactions due to their vicinity, with combination of material properties at interfaces 13 and 23 are set. Domain is discretised using five different mesh densities with uniform, square, cells, namely, 18×54, 30×90, 90×270,150×450 and 450×1350, and the cases are simulated using all three methods.

Figure 14 shows the maximum and average relative errors of displacement magnitudes for coarse meshes when compared to the displacements of the finest mesh (450×1350), for both material combinations. As can be seen, the maximum error, being always at the interface cells next to the free surface boundary, is the smallest for FAM method for all cases. On the other hand, the average error for all cases was very similar between methods, with slightly better accuracy of the FAM method.

Differences between methods in terms of stress distribution along the interface are given for the coarsest mesh (18×54) and material combination 13 only, but similar conclusions can be drawn for other cases. Normal and shear stresses are compared with the finest mesh results and presented in Figure 15. It can be seen that all methods do well again except near the free surface boundary. In terms of normal stresses the interpolation method seems to have the smallest maximum error, whereas extrapolation and FAM methods give similar, slightly higher results. However, in terms of shear stresses, only FAM method, having the smallest error, is able to simulate physically realistic distribution, with extrapolation and interpolation methods leading to rather poor results with error higher than 20%.

So far all three presented problems were modelled using structured hexagonal meshes due to simple problems' geometries. However, in reality many problems have complex geometry, for which is difficult to produce a good hexagonal mesh. Nevertheless, all three methods can also be used on unstructured meshes. To demonstrate their capabilities, the bi-material case with material combination 13 is simulated on two unstructured meshes, with trigonal and polyhedral cells, both with approximately 30 and 90 faces along vertical and horizontal edges, respectively. The trigonal mesh (Fig.16a), containing 6070 cells, is produced in *Gambit* and converted to OpenFOAM using *fluentMeshToFoam* utility, whereas the polyhedral mesh, containing 3187 cells (Fig.16b) is generated using existing trigonal meshes of both material domains by means of *polyDualMesh*, *mergeMesh* and *stitchMesh* utilities in OpenFOAM.

As can be seen in Figure 17, where stresses for all three methods and both mesh types are compared with the fine hexagonal mesh stresses, the results are

in the line with previous results on structured meshes, with FAM having better overall accuracy in terms of normal and shear stresses along the interface. It is, however, important to mention that simulations on polyhedral mesh were 50% faster than those on trigonal mesh due to less computational cells, but with similar maximum and average error in terms of displacements and stresses throughout computational domain. The accuracy of both is of the same order as for corresponding hexagonal mesh errors.

5 Conclusions

A finite volume based application for stress analysis of multi-material domain problems with accurate calculation of stresses at the material interface is presented. Three different methods of calculating tangential gradient of displacements at the interface, necessary for traction calculation, are considered and validated against problems given in literature. Two problems are geometrically axi-symmetric and simulate a compound bi-material cylinder, one subjected to pressure at the inner bore and the other one with tangential load applied to the outer surface. It is shown that all three methods perform well with this type of problem, producing negligible differences with analytical solutions.

All methods also agree well with published results when stress singularity near free edge is investigated by calculating stress distribution along the interface of multi-material plate subjected in tension, using refined mesh near interface between materials and near the edge. However, with coarser and more uniform mesh, interpolated procedure, *i.e.* the one where tangential gradient of displacement at the interface is obtained by linear interpolation, produces significant error near the free edge, whereas other two methods perform well. When stress distribution across the interface is investigated, it is shown that FAM method, *i.e.* finite area based method, is most accurate and produces physically realistic continuous trend, although differences near the interface are below 0.2% for the material properties considered, and can be neglected.

Bi-material plate simulations showed that FAM method produces the smallest maximum error in displacements, and is the only method to produce physically realistic trends of both normal and shear stresses along interface with coarser meshes. It is also worth noting that the average error for all methods follows the second-order accuracy in space, whereas the maximum error follow the first-order accuracy due to vicinity of boundary where the first-order accuracy discretisation schemes are imposed.

Finally, the execution times using all three methods were very similar for all simulations performed, with FAM being marginally slower than the other two (less than 5%). Therefore, it is suggested to primarily use FAM method for multi-material problems, although the extrapolated method can also be used safely for some problems (*i.e.* with thin interfaces, where interpolation method produce poorer results). It is also demonstrated that all methods can be used on unstructured meshes with no significant loss in accuracy when compared to simulations on structured meshes.

A Analytical solution of tangentially loaded bi-material cylinder

Differential equations describing a cylinder subjected to external loading in cylindrical coordinates are as follows [42]:

$$\begin{aligned} \frac{\partial \sigma_{rr}}{\partial r} + \frac{1}{r}\frac{\partial \sigma_{r\theta}}{\partial \theta} + \frac{\sigma_{rr} - \sigma_{\theta\theta}}{r} = 0 \\ \frac{\partial \sigma_{r\theta}}{\partial r} + \frac{1}{r}\frac{\partial \sigma_{\theta\theta}}{\partial \theta} + \frac{2}{r}\sigma_{r\theta} = 0 \end{aligned} \tag{A.1}$$

General solution of Eq. (A.1) in terms of stresses is given by following expressions:

$$\begin{aligned} \sigma_{rr} &= \frac{1}{r}\frac{\partial \phi}{\partial r} + \frac{1}{r^2}\frac{\partial^2 \phi}{\partial r^2} \\ \sigma_{\theta\theta} &= \frac{\partial^2 \phi}{\partial r^2} \\ \sigma_{r\theta} &= -\frac{\partial}{\partial r}\left(\frac{1}{r}\frac{\partial \phi}{\partial \theta}\right) \end{aligned} \tag{A.2}$$

where Airy stress function, ϕ, for a homogeneous isotropic cylinder, is

$$\phi = (C_1 \ln r + C_2 r^2 + C_3 r^2 \ln r + C_4)\theta \tag{A.3}$$

and C_i are integration constants.

For a bi-material cylinder, as shown in Fig.5b, above equations lead to the following expressions for stresses

$$\begin{aligned} \sigma_{rr}^{(k)} &= \left(\frac{C_1^{(k)}}{r^2} + 2C_2^{(k)} + C_3^{(k)} + 2C_3^{(k)} \ln r\right)\theta \\ \sigma_{\theta\theta}^{(k)} &= \left(-\frac{C_1^{(k)}}{r^2} + 2C_2^{(k)} + 3C_3^{(k)} + 2C_3^{(k)} \ln r\right)\theta \\ \sigma_{r\theta}^{(k)} &= -\frac{C_1^{(k)}(1 - \ln r) + C_2^{(k)} r^2 + C_3^{(k)} r^2 (1 + \ln r) - C_4^{(k)}}{r^2} \end{aligned} \tag{A.4}$$

and displacements

$$\begin{aligned} u_r^{(k)} &= -\frac{\theta(C_1^{(k)} + r^2 C_3^{(k)})}{2\mu^{(k)} r} + f(\theta)^{(k)} \\ u_\theta^{(k)} &= \frac{r\theta^2 C_3^{(k)}}{2\mu^{(k)}} - \int f(\theta)^{(k)} d\theta + f_1(\theta)^{(k)} \end{aligned} \tag{A.5}$$

where

$$f_1(\theta)^{(k)} = -\frac{C_1^{(k)} \ln r}{2\mu^{(k)} r} - \frac{C_2^{(k)} r \ln r}{\mu^{(k)}} - \frac{C_3^{(k)} r \ln r (1 + \ln r)}{2\mu^{(k)}} - \frac{C_4^{(k)}}{2\mu^{(k)} r} + r C_5^{(k)} \tag{A.6}$$

$$f(\theta)^{(k)} = C_6^{(k)} \sin(\theta) + C_7^{(k)} \cos(\theta) \tag{A.7}$$

and k is a material index (1 or 2 in this case).

Using boundary conditions

$$u_r^{(1)}|_{r_1} = u_\theta^{(1)}|_{r_1} = 0 \qquad \sigma_{rr}^{(2)}|_{r_3} = 0 \tag{A.8}$$

and the condition of displacement continuity at the interface, it can be shown that integration constants $C_i^{(k)}$ are all equal 0 for $i = 1, 2, 3, 6, 7$ and $k = 1, 2$. As a consequence, it follows that $u_r = 0$, $\sigma_{rr} = \sigma_{\theta\theta} = 0$ throughout cylinder. Using boundary condition $\sigma_{r\theta}|_{r_3} = \tau$, and determining $C_4^{(k)}$ constants, one can obtain the expression for shear stress profile in a bi-material cylinder, being independent on shear modulus:

$$\sigma_{r\theta}(r) = \tau \frac{r_3^2}{r^2} \tag{A.9}$$

Now, using $u_\theta^1|_{r_1} = 0$ and $u_\theta^1|_{r_2} = u_\theta^2|_{r_2}$, the only unknown constants, $C_5^{(k)}$, can be obtained, and hence the solution for circumferential displacement as:

$$u_\theta(r) = \begin{cases} \dfrac{\tau r_3^2}{2\mu_1} \left(\dfrac{r}{r_1^2} - \dfrac{1}{r} \right) & , r_1 \le r < r_2 \\ \dfrac{\tau r_3^2}{2} \left[\left(\dfrac{1}{\mu_1 r_1^2} - \dfrac{1}{\mu_1 r_2^2} + \dfrac{1}{\mu_2 r_2^2} \right) r - \dfrac{1}{\mu_2} \dfrac{1}{r} \right] & , r_2 \le r \le r_3 \end{cases} \tag{A.10}$$

References

[1] I. Demirdžić, D. Martinović, A. Ivanković, Numerical simulation of thermal deformation in welded workpiece (in Croatian), Zavarivanje 31 (1988) 209–219.

[2] I. Demirdžić, S. Muzaferija, Finite volume method for stress analysis in complex domains, International journal for numerical methods in engineering 37 (1994) 3751–3766.

[3] I. Demirdžić, S. Muzaferija, Numerical method for coupled fluid flow, heat transfer and stress analysis using unstructured moving meshes with cells of arbitrary topology, Computer methods in applied mechanics and engineering 125 (1995) 235–255.

[4] I. Demirdžić, S. Muzaferija, M. Perić, Benchmark solutions of some structural analysis problems using finite-volume method and multigrid acceleration, International journal for numerical methods in engineering 40 (1997) 1893–1908.

[5] I. Demirdžić, D. Martinović, Finite volume method for thermo-elastoplastic stress analysis, Computer methods in applied mechanics and engineering 109 (1993) 331–349.

[6] I. Demirdžić, E. Džaferović, A. Ivanković, Finite-volume approach to thermoviscoelasticity, Numerical heat transfer, Part B 47 (3) (2005) 213–237.

[7] I. Bijelonja, I. Demirdžić, S. Muzaferija, A finite volume method for incompressible linear elasticity, Computer methods in applied mechanics and engineering 195 (44-47) (2006) 6378–6390.

[8] I. Bijelonja, I. Demirdžić, S. Muzaferija, A finite volume method for large strain analysis of incompressible hyperelastic materials, International journal for numerical methods in engineering 64 (2005) 1594–1609.

[9] A. Ivanković, I. Demirdžić, J. G. Williams, P. S. Leevers, Application of the finite volume method to the analysis of dynamic fracture problems, International journal of fracture 66 (4) (1994) 357–371.

[10] A. Ivanković, S. Muzaferija, I. Demirdžić, Finite volume method and multigrid acceleration in modelling of rapid crack propagation in full-scale pipe test, Computational mechanics 20 (1-2) (1997) 46–52.

[11] V. Stylianou, A. Ivanković, Finite volume analysis of dynamic fracture phenomena - I. A node release methodology, International journal of fracture 113 (2) (2002) 107–123.

[12] V. Stylianou, A. Ivanković, Finite volume analysis of dynamic fracture phenomena - II. A cohesive zone type methodology, International journal of fracture 113 (2) (2002) 125–151.

[13] A. Ivanković, K. Pandya, J. Williams, Crack growth predictions in polyethylene using measured traction-separation curves, Engineering Fracture Mechanics 71 (4-6) (2004) 657–668.

[14] N. Murphy, A. Ivanković, The prediction of dynamic fracture evolution in PMMA using a cohesive zone model, Engineering Fracture Mechanics 72 (6) (2005) 861–875.

[15] N. Murphy, M. Ali, A. Ivanković, Dynamic crack bifurcation in PMMA, Engineering Fracture Mechanics 73 (16) (2006) 2569–2587.

[16] A. Karac, B. R. K. Blackman, V. Cooper, A. J. Kinloch, S. Rodriguez Sanchez, W. S. Teo, A. Ivankovic, Modelling the fracture behaviour of adhesively-bonded joints as a function of test rate, Engineering Fracture Mechanics 78 (2011) 973–989.

[17] A. Karac, A. Ivankovic, Modelling the drop impact behaviour of fluid-filled polyethylene containers, Fracture of Polymers, Composites and Adhesives II, ESIS Publication 32 (2003) 253–264.

[18] A. Karac, A. Ivankovic, Investigating the behaviour of fluid-filled polyethylene containers under base drop impact: a combined experimental/numerical approach, International Journal of Impact Engineering 36 (4) (2009) 621–631.

[19] V. Kanyanta, A. Ivankovic, A. Karac, Validation of a fluid-structure interaction numerical model for predicting flow transients in arteries, Journal of Biomechanics 42 (11) (2009) 1705–1712.

[20] Y. D. Fryer, C. Bailey, M. Cross, C. H. Lai, A control volume procedure for solving elastic stress-strain equations on an unstructured mesh, Applied mathematical modelling 15 (11-12) (1991) 639–645.

[21] C. Bailey, M. Cross, A finite-volume procedure to solve elastic solid mechanics problems in three dimensions on an unstructured mesh, International journal for numerical methods in engineering 38 (10) (1995) 1757–1776.

[22] G. A. Taylor, C. Bailey, M. Cross, Solution of the elastic/visco-plastic constitutive equations: a finite volume approach, Applied mathematical modelling 19 (12) (1995) 746–760.

[23] N. A. Fallah, C. Bailey, M. Cross, G. A. Taylor, Comparison of finite element and finite-volume methods application in geometrically nonlinear stress analysis, Applied mathematical modelling 24 (7) (2000) 439–455.

[24] G. A. Taylor, C. Bailey, M. Cross, A vertex-based finite-volume method applied to nonlinear material problems in computational solid mechanics, International journal for numerical methods in engineering 56 (4) (2003) 507–529.

[25] G. Kluth, B. Després, Discretization of hyperelasticity on unstructured mesh with a cell-centered Lagrangian scheme, Journal of Computational Physics 229 (24) (2010) 9092–9118.

[26] G. Kluth, B. Després, Discretization of hyperelasticity on unstructured mesh with a cell-centered Lagrangian scheme, Journal of Computational Physics 229 (24) (2010) 9092–9118.

[27] G. Carre, S. Del Pino, B. Després, E. Labourasse,, A cell-centered Lagrangian hydrodynamics scheme on general unstructured meshes in arbitrary dimension, Journal of Computational Physics 228(14) (2009) 51605183.

[28] M. A. Wheel, A geometrically versatile finite volume formulation for plane elastostatic stress analysis, The Journal of Strain Analysis for Engineering Design 31 (2) (1996) 111–116.

[29] M. A. Wheel, A mixed finite volume formulation for determining the small strain deformation of incompressible materials, International Journal for Numerical Methods in Engineering 44 (12) (1999) 1843–1861.

[30] P. Wenke, M. A. Wheel, A finite volume method for solid mechanics incorporating rotational degrees of freedom, Computers and structures 81 (5) (2003) 321–329.

[31] M. A. Wheel, A finite volume method for analysing the bending deformation of thick and thin plates, Computer Methods in Applied Mechanics and Engineering 147 (1-2) (1997) 199–208.

[32] H. G. Weller, G. Tabor, H. Jasak, C. Fureby, A tensorial approach to computational continuum mechanics using object orientated techniques, Computers in physics 12 (6) (1998) 620–631.

[33] H. Jasak, H. G. Weller, Application of the finite volume method and unstructured meshes to linear elasticity, International journal for numerical methods in engineering 48 (2000) 267–287.

[34] J. H. Ferziger, M. Perić, Computational methods for fluid dynamics, Springer Verlag, Berlin-New York, 1995.

[35] H. Jasak, Error analysis and estimation for finite volume method with applications to fluid flows, Ph.D. thesis, Imperial College, University of London (1996).

[36] D. A. Edwards, H. Brenner, D. T. Wasan, Interfacial transport processes and rheology, Butterworth-Heinemann, 1991.

[37] C. E. Weatherburn, Differential geometry in three dimension, Cambridge University Press, London, 1972.

[38] Ž. Tuković, H. Jasak, A moving mesh finite volume interface tracking method for surface tension dominated interfacial fluid flow, Computers and fluids, 55 (2012) 70–84.

[39] Ž. Tuković, Finite volume method on domains of varying shape (in Croatian), Ph.D. thesis, Faculty of Mechanical Engineering and Naval Architecture, University of Zagreb (2005).

[40] D. A. H. Jacobs, Preconditioned Conjugate Gradient methods for solving systems of algebraic equations, Tech. Rep. RD/L/N193/80, Central Electricity Research Laporatories (1980).

[41] A.-V. Phan, S. Mukherjee, The multi-domain boundary contour method for interface and dissimilar material problems, Engineering Analysis with Boundary Elements 33 (2009) 668–677.

[42] G. Nie, R. C. Batra, Material tailoring and analysis of functionally graded isotropic and incompressible linear elastic cylinders, Composite structures 92 (2010) 265–274.

[43] S. Ioka, K. Masuda, S. Kubo, Singular stress field near the edge of interface of bonded dissimilar materials with an interlayer, International Journal of Solids and Structures 44 (2007) 6232–6238.

[44] D. Bogy, On the problem of edge-bonded elastic quarter-palnes loaded at the boundary, International Journal of Solids and Structures (1970) 1287–1313.

List of Figures

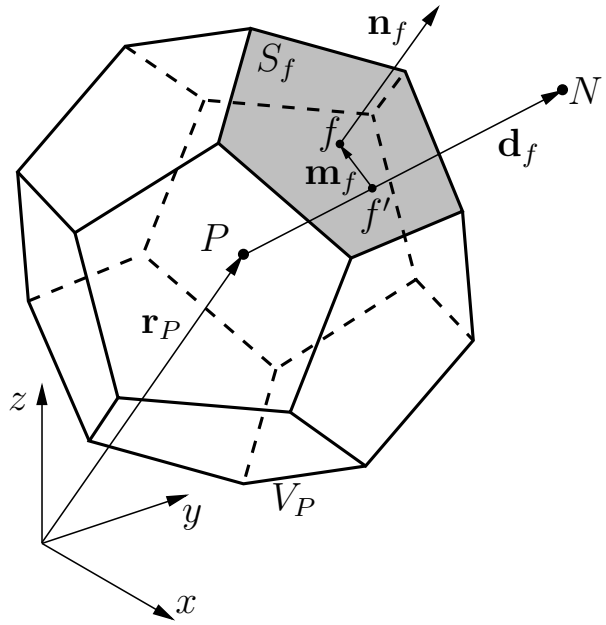

Figure 1: Polyhedral control volume (cell).

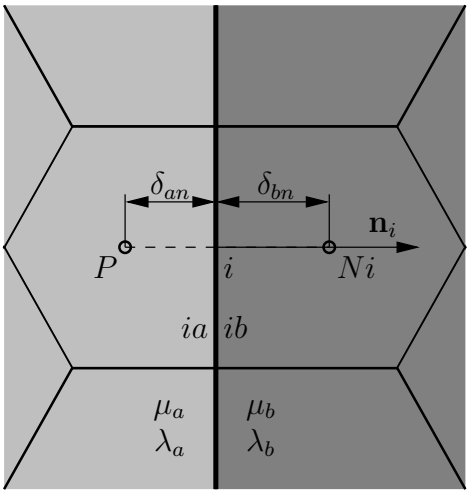

Figure 2: Control volumes V_P and V_{Ni} sharing face i at the multi-material interface.

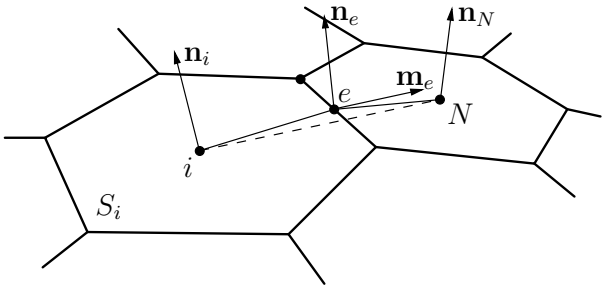

Figure 3: Control area S_i at the interface.

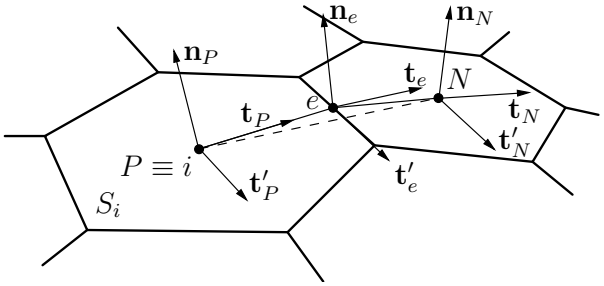

Figure 4: Edge-based local orthogonal coordinate system whose axes are aligned with orthogonal unit vectors $\mathbf{n}$, $\mathbf{t}$ and $\mathbf{t}'$, where vector $\mathbf{t}$ is tangential to the geodetic line $\overline{PeN}$.

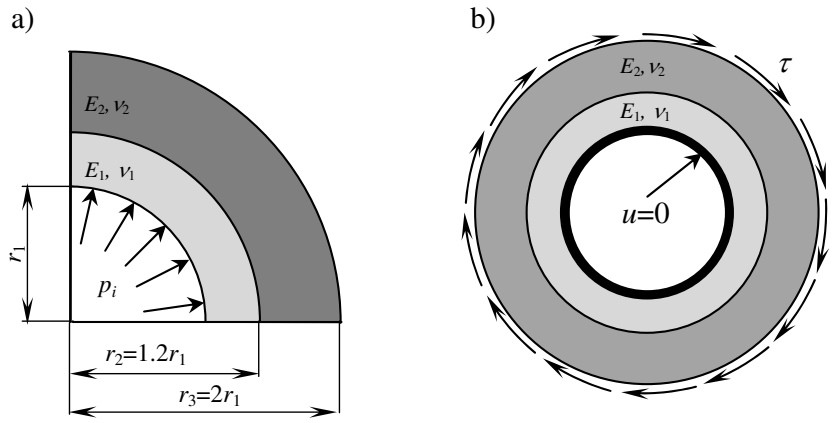

Figure 5: Geometry of compound cylinder problems: a) internal pressure applied b) tangential loading applied

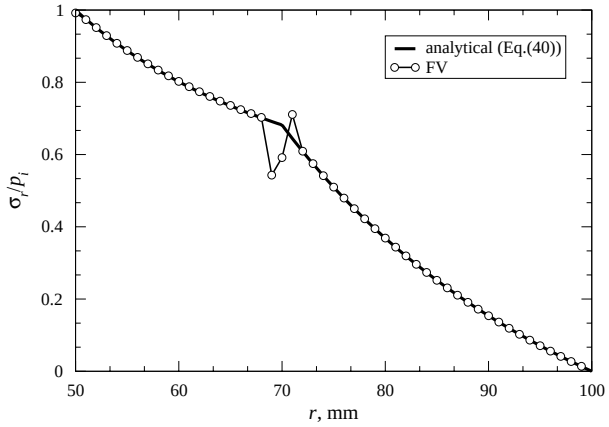

Figure 6: Stress distribution of radial stress, σ_r, without special treatment in traction calculation at the interface

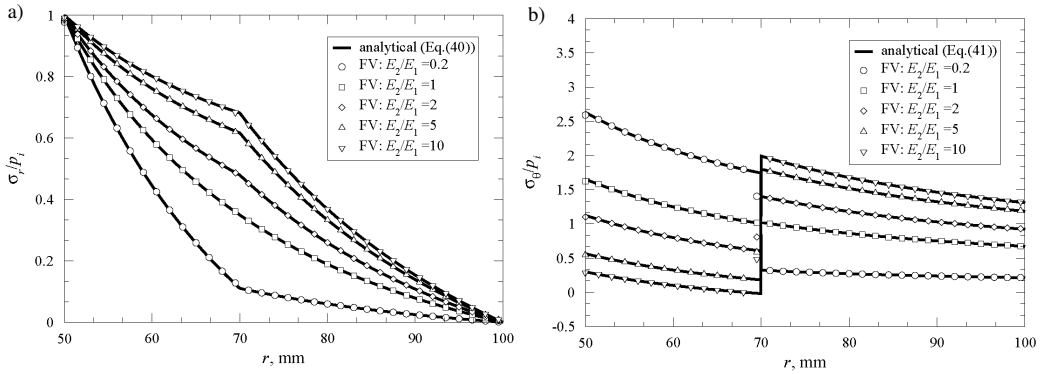

Figure 7: Stress distribution in pressurised cylinder: a) radial stress, σ_r, b) circumferential stress, σ_θ

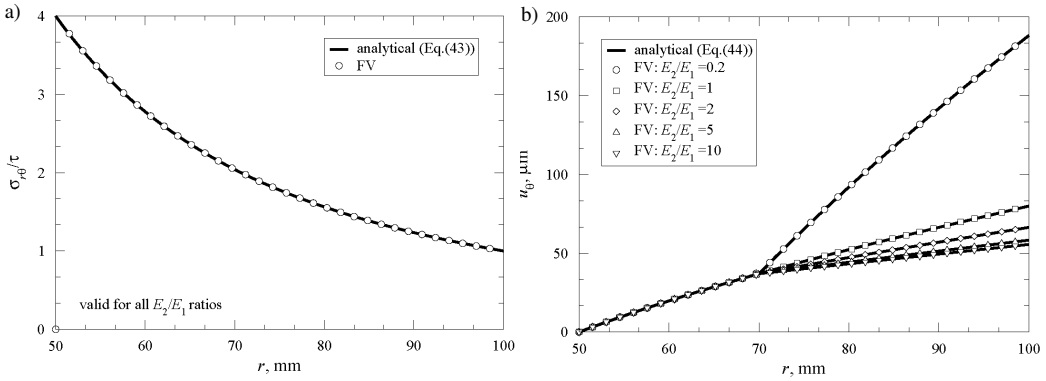

Figure 8: Stress distribution in tangentially loaded cylinder: a) shear stress, $\sigma_{r\theta}$, b) circumferential displacement, u_θ

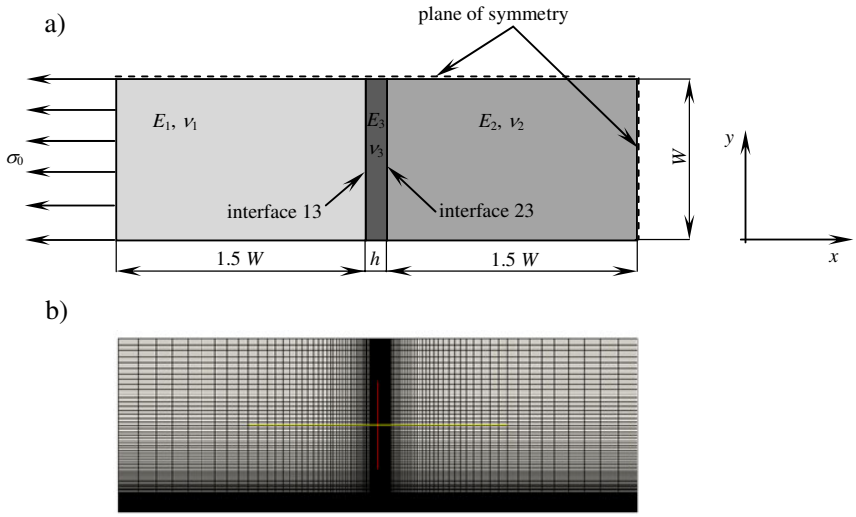

Figure 9: Multi-material plate: a) geometry b) mesh

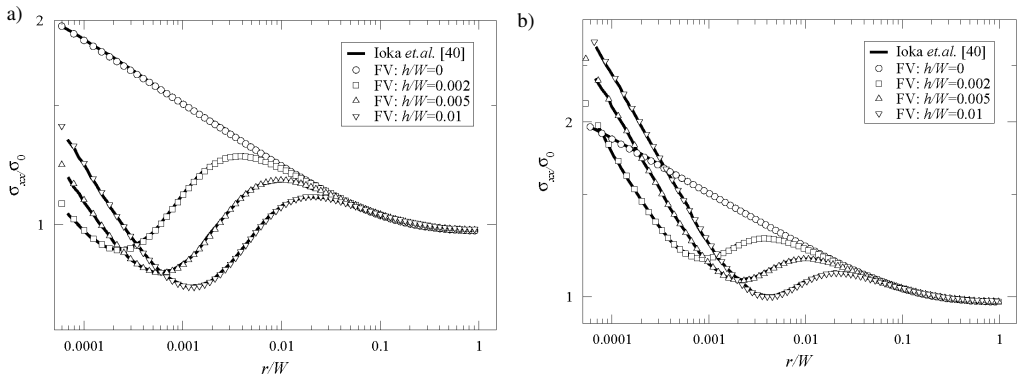

Figure 10: Normal stress distribution along interfaces: a) Interface 13 b) Interface 23

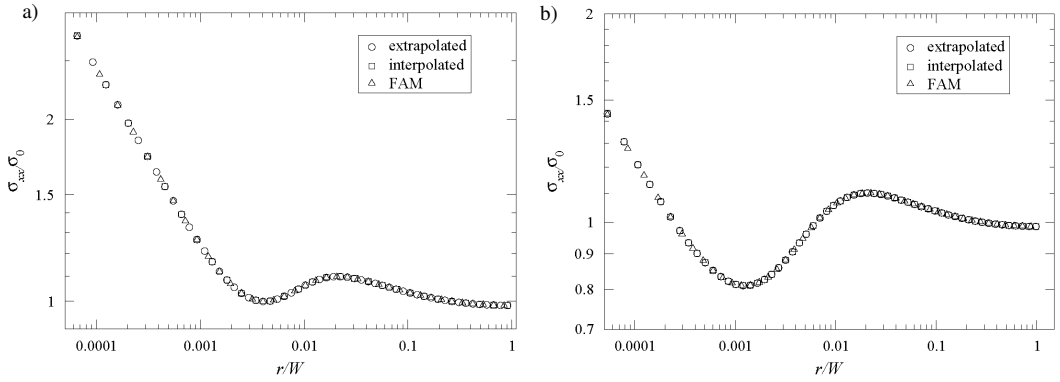

Figure 11: Stress distribution along interfaces for finer mesh ($h = 0.01W$): a) Interface 13 b) Interface 23

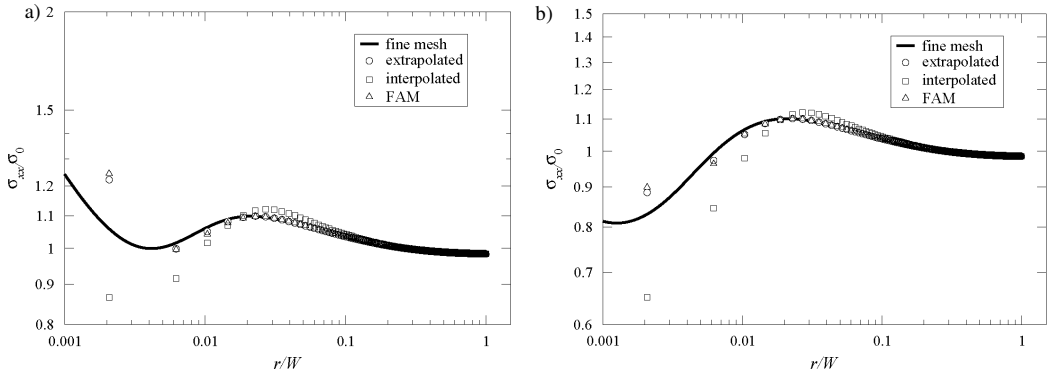

Figure 12: Stress distribution along interfaces for coarser mesh ($h = 0.01W$): a) Interface 13 b) Interface 23

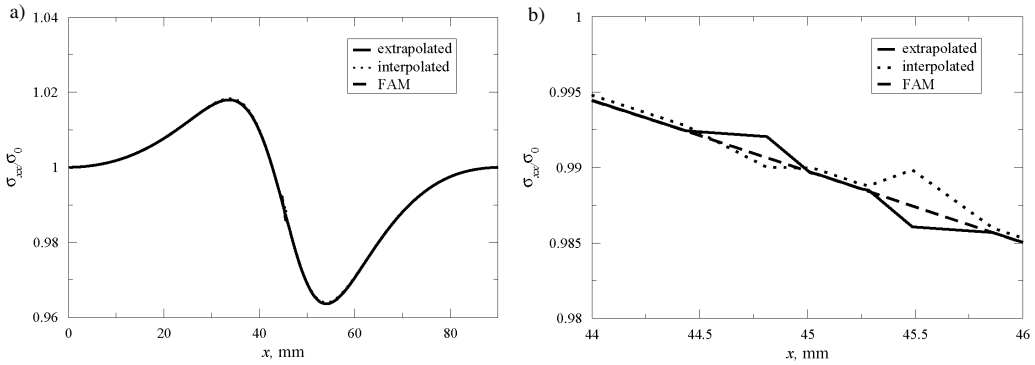

Figure 13: Stress distribution along mid-line for coarse mesh ($h = 0.01W$)

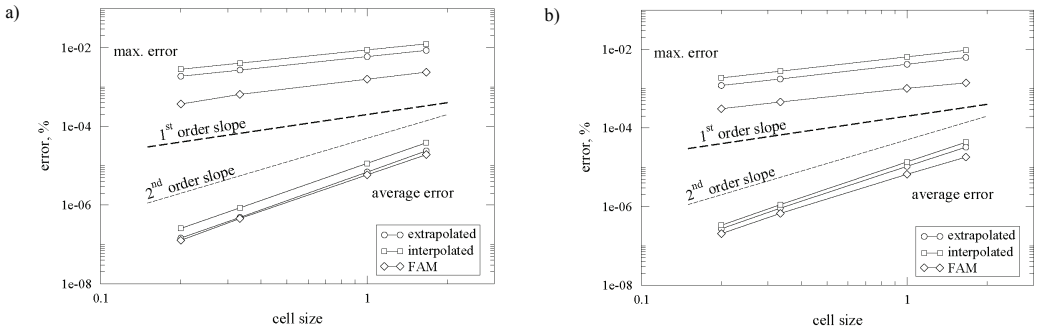

Figure 14: Error analysis for bi-material case: a) Material combination 13, b) Material combination 23

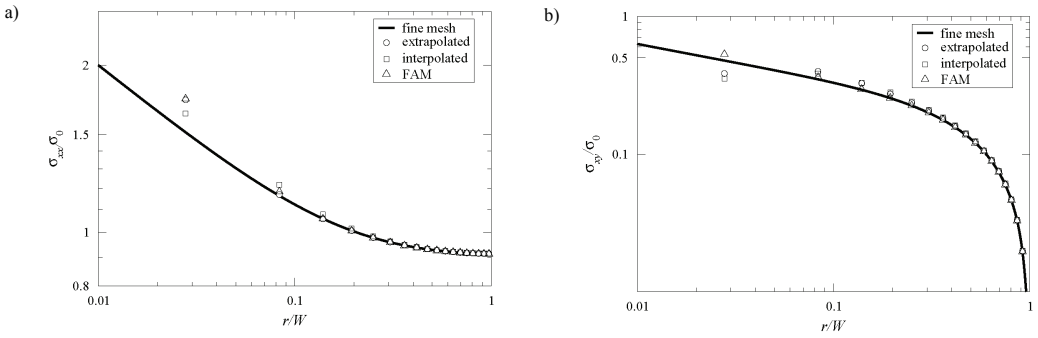

Figure 15: Stress distribution along the interface for bi-material cases: a) Normal stress b) Shear stress

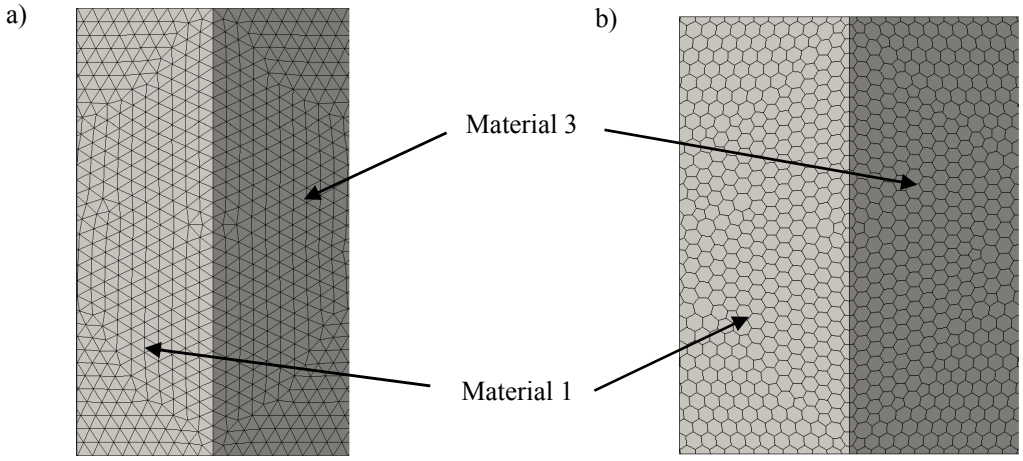

Figure 16: Segments of unstructured meshes for bi-material case: a) Trigonal cells b) Polyhedral cells

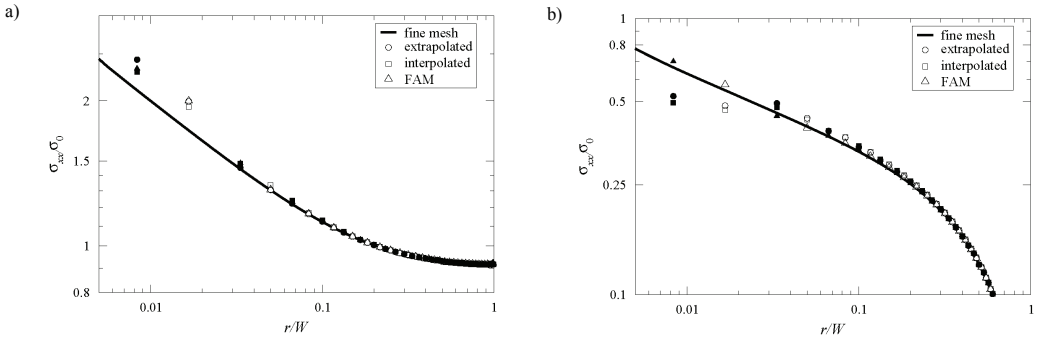

Figure 17: Stress distribution for bi-material unstructured mesh cases: a) Normal stress b) Shear stress (empty symbols: trigonal, filled symbols: polyhedral)

List of Tables

Property	Material 1	Material 2	Material 3
E, GPa	206.0	70.3	4.93
ν, -	0.300	0.345	0.330

Table 1: Material properties used in example 4.3